Met. Mater. Int., Vol. 20, No. 1 (2014), pp. 105~111
doi: 10.1007/s12540-013-6013-z

Effects of Atomic Size Difference and Heat of Mixing Parameters on the Local Structure of a Model Metallic Glass System

Y. S. Yun[1], H. S. Nam[2], P.-R. Cha[2], W. T. Kim[3], and D. H. Kim[1,*]

[1]Yonsei University, Center for Non-crystalline Materials, Department of Metallurgical Engineering, Seoul 120-749, Korea
[2]Kookmin University, School of Advanced Materials Engineering, Seoul 136-702, Korea
[3]Cheongju University, Department of Optical Engineering, Cheongju 360-764, Korea

(received date: 16 January 2013 / accepted date: 14 May 2013)

Atomic size differences between constituting elements and the heat of mixing are key factors in designing a metallic glass system. In this study, the effects of atomic size differences and the heat of mixing on the glass-forming ability and the local structure of metallic glasses were studied via molecular dynamic simulations of an ideal system known as the Lennard-Jones embedded-atom method model. The atomic size difference and the heat of mixing of the system were varied by means of the Lennard-Jones parameters. The glass transition behavior was characterized based on the chemical short-range order and by a Voronoi analysis. Our simulations lead to optimized windows of atomic size differences and heat of mixing parameters for metallic glass-forming of the model system. Both a greater negative heat of mixing and a larger atomic size difference are necessary for the enhancement of the glass-forming ability.

Key words: computer simulation, glasses, metals, ordering, crystallization

1. INTRODUCTION

Metallic glasses have drawn much attention due to their unique mechanical properties. Due to the absence of a long-range order in its atomic structure, metallic glass (MG) shows a high yield strength, a large elastic limit (~2%) and limited plasticity, especially in tensile mode. Although significant progress has been made in developing new alloy systems with degrees of high glass-forming ability (GFA), most experiments are based on three empirical rules for a high GFA: a multi-component system, a considerable degrees of negative heat of mixing and a large difference in the atomic size between the constituting elements [1,2]. For the transition from the liquid phase to glass, it is necessary to suppress the nucleation and growth of the competing crystalline phase. From the viewpoint of thermodynamics and kinetics, this can be achieved through stabilization of the liquid phase by forming a densely packed liquid structure [3]; destabilizing the competing crystalline phase by introducing large elastic strain energy [3,4]; and by forming new local atomic configurations in liquid, such as icosahedral clusters [5,6], which are completely different from those of the corresponding crystalline phases.

*Corresponding author: dohkim@yonsei.ac.kr

Although the empirical rules for GFA are widely accepted ideas, it is difficult to observe experimentally the direct effects of the atomic size difference and heat of mixing on the GFA and local atomic structure: Because there are diverse types of alloys that exhibit glass phases with different bonding characteristics and phase equilibrium behavior, it is difficult to find a direct and qualitative relationship between GFA and the atomic-level characteristics. In order to overcome the complexity of experimental data analysis [7,8], many theoretical studies have been performed, mostly based on ideal models such as a hard sphere or Lennard-Jones (LJ) glass [9-13]. However, these ideal systems use simple pair potential models while neglecting the many-body characteristic of metallic bonding. Therefore, the tendency drawn from a hard sphere or from LJ glasses may not be directly comparable with trends in real metallic glasses.

There have also been a number of molecular dynamics studies of GFA based on embedded-atom method (EAM) models [14-33]. However, because the models are matched to particular alloy systems, these previous works are not appropriate to explain the general effects of atomic size differences and the heat of mixing on GFA in metallic glass systems. Hence, an explanation of the atomic size and heat of mixing effects based on empirical trends needs to be reinvestigated systematically with realistic models appropriate for metallic systems. In this study, molecular dynamics (MD)

simulations were employed to resolve the effects of the atomic size difference and interatomic bond strength on the GFA and local atomic structure during quenching and in a quenched state. Because many parameters operate simultaneously in a real system, it is difficult to isolate the effects of the atomic size difference and heat of mixing separately from other parameters. Here, instead of considering a complex alloy system, we chose an ideal system known as the Lennard-Jones embedded-atom method (LJ-EAM) [34-43]. This model system has been used to describe the main features of metallic systems with the two parameters of the equilibrium interatomic distance and the potential well-depth [34-43]. Therefore, the LJ-EAM is considered to be suitable to analyze the effects of the atomic size and heat of mixing parameters on GFA and local structure changes independently in metallic glass systems. (Furthermore, due to its simple form, this model is easily extendable to multi-component systems.) Here, through molecular dynamics simulations based on the LJ-EAM models, we calculated various structural properties of LJ-EAM glasses, including the lattice crystallinity and fraction of icosahedral clusters as a function of the adjustable potential parameters of the atomic size and potential well depth.

2. EXPERIMENTAL PROCEDURES

2.1. Interatomic potentials

In order to investigate the effects of various atomic size ratios and heat of mixing parameters, MD simulations were carried out based on the LJ-EAM potential model. Like the Lennard-Jones system, the LJ-EAM model has two physical parameters: the equilibrium interatomic distance $r(=\sqrt[6]{2}\sigma)$ and the potential well-depth ε [33]. However, unlike the Lennard-Jones system, the LJ-EAM model represents metallic bond characteristics by introducing the many-body interaction formalism of the embedded atomic method (EAM) model [33].

For a binary material described by classical LJ pair potentials, the interatomic potentials between atoms i and j take the form

$$\phi^{LJ}_{S_iS_j} = 4\varepsilon_{S_iS_j}\left[\left(\frac{\sigma_{S_iS_j}}{r}\right)^{12} - \left(\frac{\sigma_{S_iS_j}}{r}\right)^{6}\right], \quad (1)$$

where $\varepsilon_{S_iS_j}$ and $\sigma_{S_iS_j}$ correspond to the attractive well depth and the diameter for the LJ potential describing the interactions between species S_i and S_j ($S = A$ or B). The total energy E of a binary LJ-EAM system is given by the usual EAM form [33].

$$E = \Sigma_i F_{S_i}(\bar{\rho}_i) + \frac{1}{2}\Sigma_{j\neq i}\phi_{S_iS_j}(r_{ij}) \quad (2)$$

where $F_{S_i}(\bar{\rho}_i)$ is the embedding energy and $\phi_{S_iS_j}(r_{ij})$ is the pair interaction term between atoms i and j separated by distance r_{ij}. For $F(\bar{\rho})$, we set the parameters of many-body bonding and the decay of the electron density to 0.8 and 6.0, respectively, such that the model alloys exhibit an equilibrium solid state of a face-centered cubic structure. A more detailed description of the functional form of $F_{S_i}(\bar{\rho}_i)$ and $\phi_{S_iS_j}(r_{ij})$ in the LJ-EAM model can be found in the literature [33].

2.2. Simulation procedure

All of the simulations were carried out based on the LJ-EAM potential model. First, we arbitrarily set the equilibrium interatomic distance of *A-A* pairs, $r_A(=\sqrt[6]{2}\sigma_{AA})$, to 3.2 Å. We chose a potential well-depth $\varepsilon_{AA} = \varepsilon_{BB} = 0.5$ eV for both species *A* and *B*. Then, by changing the atomic size parameter $r_B(=\sqrt[6]{2}\sigma_{BB})$ and pair interaction parameter ε_{AB}, various LJ-EAM alloys were designed. Here, we define the atomic size ratio $r_{B/A} = r_B/r_A$ and heat of mixing parameter $\varepsilon_{AB/AA} = \varepsilon_{AB}/\varepsilon_{AA}$ or $\varepsilon_{AB}/\varepsilon_{BB}$. By setting $r_{B/A}$=1.00, 0.95, 0.90, 0.85, and 0.80 and $\varepsilon_{AB/AA}$=0.90, 0.95, 1.00, 1.05, 1.10, 1.15, and 1.20, a total of 35 (=5×7) alloy systems of different ($r_{B/A}$, $\varepsilon_{AB/AA}$) combinations were generated. Then, LJ-EAM alloys can be expressed as ($r_{B/A}$, $\varepsilon_{AB/AA}$) on the (x, y) plane, where x is the $r_{B/A}$ value and y is the $\varepsilon_{AB/AA}$ value. For the set of alloy systems represented by ($r_{B/A}$, $\varepsilon_{AB/AA}$), the heat of mixing was calculated by molecular static simulations. Next, in order to evaluate the GFA, MD simulations of the quenching process were carried out as follows: simulation cells containing 10,976 atoms with a periodic boundary condition in all three dimensions were generated. The samples were melted and equilibrated at 2000 K (well above the melting temperature) for 1 ns (where the time step $\Delta t = 2.5$ fs) and quenched into glassy states (T=50 K) at a cooling rate of 10^{11}K/s, after which they were annealed (T=50 K). Finally, the structures were characterized based on the chemical short-range order (CSRO) and a Voronoi analysis.

3. RESULT

3.1. Heat of mixing

The heat of mixing was calculated by computing the internal energy difference between the solid solution and pure components at 0 K as follows:

$$\Delta H_{mix} = E_{mix} - (X_A E_A + X_B E_B) \quad (3)$$

Here, E_{mix}, E_A and E_B are the internal energies of the randomly mixed fcc solid solution and of pure *A* and *B*, respectively, and X_A and X_B are the mole fractions of the *A* and *B* components, respectively. Also, the heat of mixing can be estimated using a regular solution model with the interaction energy parameter ε between the *A-A*, *B-B*, and *A-B* pairs. Figure 1(a) shows the composition dependences of ΔH_{mix} for $r_{B/A}$=1.0 calculated at various interaction parameters $\varepsilon_{AB/AA}$ ranging from 0.9 to 1.2. In this graph, the symbols represent the results of molecular

static simulations for randomly mixed alloy structures with lattice relaxation and the solid lines represent the results of the regular solution model. With the same atomic size of $r_{B/A}$ =1.0, the results of the random-mixing simulations are not very different from those of the regular solution model. They are symmetric with respect to the composition, as the *A* and *B* atoms are of the same size. When $\varepsilon_{AB/AA}$=1, ΔH_{mix}=0, as the bond strength of the *A*-*B* pair is identical to that of the *A*-*A* and *B*-*B* pairs and because *A* and *B* are chemically identical, or isotopes. However, when $\varepsilon_{AB/AA}$ is not equal to 1, the regular solution model slightly underestimates the absolute value of the heat of mixing compared to the calculated value of ΔH_{mix} for both attractive ($\varepsilon_{AB/AA}$>1.0) and repulsive ($\varepsilon_{AB/AA}$<1) cases. The slight difference between the calculated values and those predicted by the regular solution model may be understood by the effect of the many-body interactions of the LJ-EAM model.

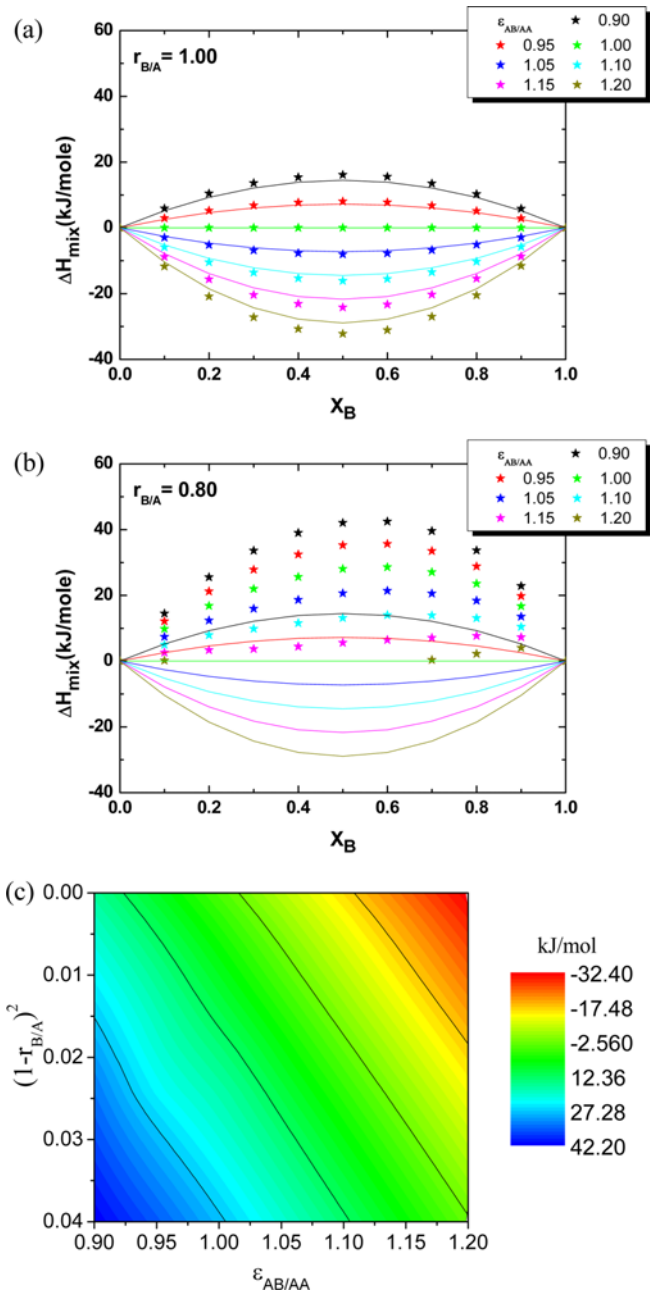

Fig. 1. Composition dependences of ΔH_{mix}: (a) for $r_{B/A}$=1.0 and (b) for $r_{B/A}$=0.8, calculated with various interaction parameters $\varepsilon_{AB/AA}$, (star symbol for the molecular static simulation, solid line for the regular solution model); and (c) heat of mixing of the $A_{50}B_{50}$ alloy plotted on the coordinate space of $(1-r_{B/A})^2$ and $\varepsilon_{AB/AA}$ with iso-lines of ΔH_{mix}.

Figure 1(b) shows the composition dependences of ΔH_{mix} for $r_{B/A}$=0.8 at various interaction parameters $\varepsilon_{AB/AA}$ ranging from 0.9 to 1.2. In this graph, it can be noted that the calculated heat of mixing is much larger than the estimated values according to the regular solution model for all calculated conditions irrespective of the attractive or repulsive interactions between the A-B pairs. This result clearly indicates that the atomic size difference plays a role in increasing the internal energy of the crystalline solid solution [4]. The regular solution model assumes the atomic bond length to be constant based on a fixed lattice model and only considers the internal energy contributed by the chemical interaction energy between two components. However, in an actual situation, the crystal lattice of a random-mixing alloy should be distorted and the atomic size mismatch leads to an increase of the internal energy, which corresponds to the elastic strain energy stored in the solid solution. For the same reason, even when $\varepsilon_{AB/AA}$=1, the system exhibits large positive heat of mixing due to the large size difference. Also, it should be noted that the calculated ΔH_{mix} is fairly non-symmetric with respect to the composition [11].

Figure 1(c) shows the distribution of ΔH_{mix} for $A_{50}B_{50}$ alloys for various LJ-EAM systems plotted on the coordinate space of $(1-r_{B/A})^2$ and $\varepsilon_{AB/AA}$. The iso-lines of $\ddot{A}H_{mix}$ are also included for various positive and negative ΔH_{mix} values. The iso-lines appear to be straight lines in the $(1-r_{B/A})^2-\varepsilon_{AB/AA}$ coordinate space, implying that ΔH_{mix} is a simple linear function of $(1-r_{B/A})^2$ and $(1-\varepsilon_{AB/AA})$.

3.2. Quenching process

Figure 2 shows snapshots of the atomic structure analyzed by the coordination number analysis (CNA) method [44] for selected LJ-EAM systems: ($r_{B/A}$, $\varepsilon_{AB/AA}$) = (1, 0.9), (1, 1.2), (0.8, 0.9) and (0.8, 1.2) at different temperatures during a rapid cooling process. Only some selected atomic configurations of high crystallinity, including fcc, hexagonal closed-packed (hcp), body-centered cubic (bcc) and icosahedrons clusters, are displayed for convenience. In alloys with the same atomic size, $r_{B/A}$=1.00, fcc, hcp, bcc type atomic configuration appears, indicating that these alloys have poor GFA characteristics regardless of their heat of mixing properties. The formation of crystalline clusters is always preferred at lower temperatures and in both alloys having either attractive or repulsive interactions between two components.

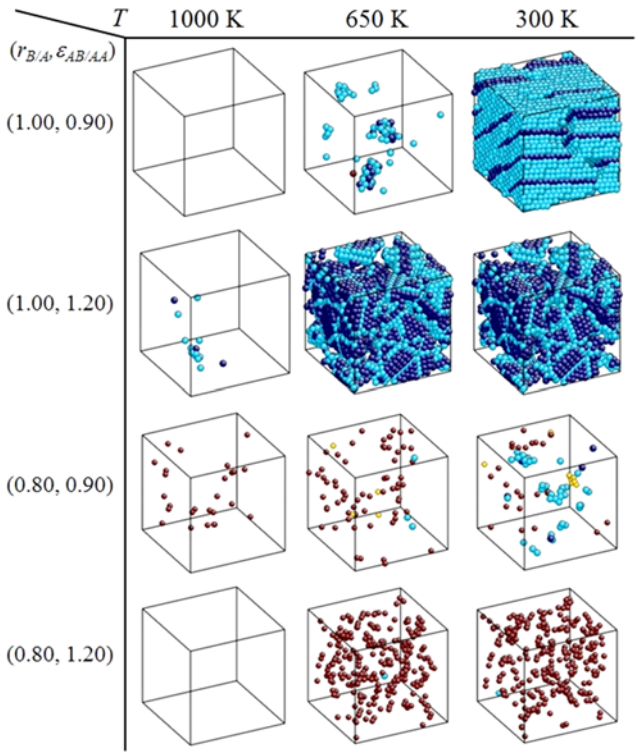

Fig. 2. Snapshot of the atomic structure as analyzed by the CNA method during the quenching process (navy: fcc, cyan: hcp, yellow: bcc, red: icosahedron).

These results strongly imply that liquid alloys consisting of elements with the same atomic size can easily crystallize by crystal nucleation during cooling. In alloys with $r_{B/A}$=0.8, clusters with an icosahedral local structure formed instead of a crystalline local structure. The popularity of icosahedral clusters is much higher in the case of a negative heat of mixing as compared to a case with a strong positive heat of mixing. Considering that the stable crystalline phase in this LJ-EAM potential is the fcc phase, a local atomic configuration such as an icosahedral cluster is far different from the local atomic configuration in the competing crystalline phase [5,6]. Therefore, the preferential formation of the icosahedral cluster can be considered as an indicator of the GFA. The high popularity of the icosahedral cluster in the alloy with $r_{B/A}$=0.8 and with $\varepsilon_{AB/AA}$=1.2 suggests that this alloy has the highest GFA among the alloys studied here.

3.3. Structure analysis

Figure 3 shows the atomic structure of the solid obtained after the quenching process. In the $\varepsilon_{AB/AA}$=0.90 case, phase separation occurred due to the repulsive interaction between two components. The atomic image of ($r_{B/A}$, $\varepsilon_{AB/AA}$) = (1.00, 0.90) shows a crystalline structure, while the atomic image of ($r_{B/A}$, $\varepsilon_{AB/AA}$) = (0.80, 0.90) shows a meta-crystalline structure. For alloys having strong attractive interaction between two components, for example $\varepsilon_{AB/AA}$=1.20, a homogeneously mixed

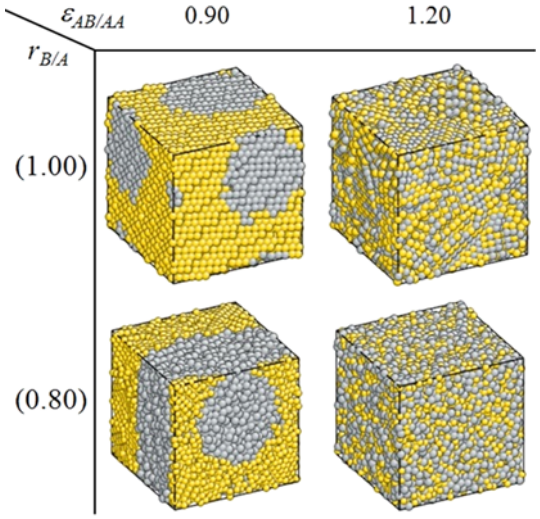

Fig. 3. Snapshot of a solid after the quenching process (50 K) (gray: A atom, yellow: B atom).

solid solution is formed. While the atomic image of ($r_{B/A}$, $\varepsilon_{AB/AA}$) = (1.00, 1.20) shows a clear crystalline structure, the atomic image of ($r_{B/A}$, $\varepsilon_{AB/AA}$) = (0.80, 1.20) shows an amorphous structure. These results show that a different atomic structure is obtained due to the atomic radius difference despite the fact that the chemical bond strength is identical. Because the effect of the atomic radius difference can essentially induce the effect of positive mixing enthalpy between the atoms, the tendency for phase separation becomes higher as the difference in the atomic radius increases. The presence of neighboring atom with a large atomic size difference raises the energy level of the crystalline state, thus destabilizing the crystalline state. Therefore, when the atomic size difference is large, the atomic structure is not in the crystalline state in spite of the occurrence of phase separation. The crystallinity of the quenched alloy was further analyzed by means of a radial distribution function (RDF) analysis.

Figure 4 is a map showing a summary of the phase evolution in quenched solid specimens, plotted in the coordinate space of $r_{B/A}$ and $\varepsilon_{AB/AA}$. The phase space can be divided basically into three regimes: phase separation, the crystalline phase, and the glass phase. Phase separation occurs mainly in alloys having a positive heat of mixing ΔH_{mix}, in good agreement with Fig. 1(c). Also, a large atomic size difference promotes the occurrence of phase separation. The crystalline phase was found when the atomic size difference is small irrespective of the interaction energy, indicating that the atomic size difference is an essential factor in improving the GFA [3]. Finally, the glass phase was found in the regimes having a large difference in the atomic size between two components and negative heat of mixing sufficient to prevent phase separation. These results are in agreement with Inoue's three empirical rules for a high GFA [1]. For a more detailed explanation, a

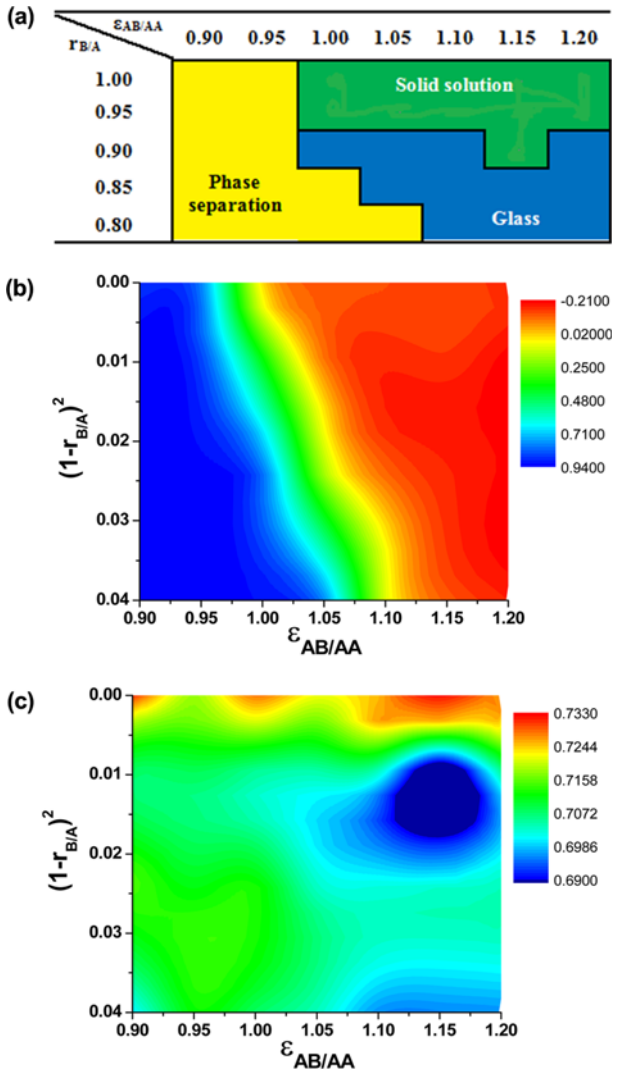

Fig. 4. (a) Distribution of the phase in a quenched solid plotted in the coordinate space of $r_{B/A}$ and $\varepsilon_{AB/AA}$. (b) a CSRO (Warren-Cowley parameter) map at $A_{50}B_{50}$. The Warren-Cowley parameter [28] is defined as $\alpha = 1 - \frac{C_{AB}}{C * X_B}$, where C is the coordination number, X_B is the atomic fraction of element B and C_{AB} is the partial coordination number of element B around element A. $\alpha>0$ indicates clustering or phase separation, whereas $\alpha<0$ denotes chemical ordering; $\alpha \sim 0$ signifies a random solution. (c) Packing density map at $A_{50}B_{50}$.

CSRO (Warren-Cowley parameter) map and a packing density map at $A_{50}B_{50}$ are shown in Figs. 4(b) and (c), respectively.

4. DISCUSSION

In this section, we discuss the variation of the heat of mixing shown in Fig. 1 as a function of the interaction energy parameter $\varepsilon_{AB/AA}$ and the atomic size difference parameter $r_{B/A}$. Figure 1(c) shows that the heat of mixing in the solution is a simple linear function of $(1-r_{B/A})^2$ and $(1-\varepsilon_{AB/AA})$; it can be expressed through the following equation:

$$\Delta H_{mix} = A(1-\varepsilon_{AB/AA}) + B(1-r_{B/A})^2 \quad (4)$$

The first and the second terms correspond to the chemical interaction energy contribution and the atomic size difference contribution, respectively. The calculated heat of mixing could be best fitted with A=156.2 kJ/mole and B=707.6 kJ/mole. The chemical interaction energy term can be estimated using a regular solution model, which gives an A value of 144.7 kJ/mole. In the regular solution model, only the first nearest interaction energy is considered, resulting in an underestimation of the heat of mixing, as shown in Fig. 1(a). Figure 1(b) shows the different degree of symmetry in the heat of mixing curves depending on the atomic size difference. The reason can be discussed as follows: firstly, the potential well curve is non-symmetric at equilibrium. When a large atom is located at the center (lattice) of small atoms with a shorter pair distance than the equilibrium distance, the internal energy change will be larger compared to when a small atom is located at the center of large atoms with a longer distance than the equilibrium distance; secondly, there is a strain difference between the two cases, i.e., when a large atom is located at the center of small atoms and when a small atom is located at the center of large atoms [11]. For example, when $r_{B/A}$ is 0.8, the compression strain of a large atom located at the center of small atoms is 25%, whereas the tensile strain of a small atom located at the center of large atoms is 20%.

Figure 4 shows that the larger atomic size difference and the larger negative heat of mixing between the two components are the main factors for a high GFA [1,45]. A greater negative heat of mixing enforces the formation of an atomic pair between different components, while the positive heat of mixing promotes the formation of an atomic pair between the same components. A large atomic size difference increases the internal energy of the crystalline solid solution, as shown in Fig. 1(b), destabilizing the crystalline phase [3,4]. As shown in Fig. 2, alloys consisting of elements of the same atomic size preferentially formed a crystalline local structure regardless of whether the chemical interaction between two components is attractive or repulsive, despite the fact that attractive interaction even promotes the formation of the crystalline phase at a higher temperature. Destabilizing the competing crystalline phase can be achieved only by preferential atomic pair formation between two components having a large difference in their atomic sizes [3,4]. Therefore, both a larger difference in the atomic size and a larger negative heat of mixing are key factors for a high GFA.

The formation of clusters with an icosahedron local structure in the liquid state may enhance the GFA of the alloy [5]. The icosahedral cluster corresponds to the densest packing configuration and is far different from the local atomic configuration in the fcc or hcp crystalline phase. Once icosahedral clusters are formed densely in the liquid state [5], the

nucleation and growth of the crystalline phase are expected to be suppressed. Therefore, the preferential formation of the icosahedral clusters can be considered as a GFA indicator [5]. Figures 5(a) and (b) show the calculated fraction of the icosahedron-centered atoms F_{ico} and the ratio of the atomic distance between the smaller and neighboring atoms as analyzed by the Voronoi method. The alloys solidified into a crystalline phase have a very small fraction of icosahedron-centered atoms, while the alloys solidified into a glass structure showed F_{ico} values that generally exceed 3%. In general, F_{ico} increases as the interaction energy parameter $\varepsilon_{AB/AA}$ and the atomic size difference increase [6]. However, the highest F_{ico} was found in the system with $(r_{B/A}, \varepsilon_{AB/AA}) = (0.80, 1.10)$ instead of the system with $(r_{B/A}, \varepsilon_{AB/AA}) = (0.80, 1.20)$. This result suggests that there is a preferential atomic size ratio during the formation of an icosahedral cluster. The existence of the preferential atomic size difference for the formation of an icosahedral cluster may be related to the geometry of the icosahedron. The theoretical ratio between the edge and the center vertex is 1/0.95 in the icosahedron structure. This ideal configuration can be achieved by forming icosahedrons with a centered-atom having an atomic radius 10% smaller than that of the neighbor atoms. However, the neighboring atoms are not always identical and an accurate prediction of the optimum atomic size ratio for the formation of icosahedral clusters is difficult. Nonetheless, the generation of the icosahedral structure requires neighboring size-mismatched elements with a ratio of 0.9 or less [4,6].

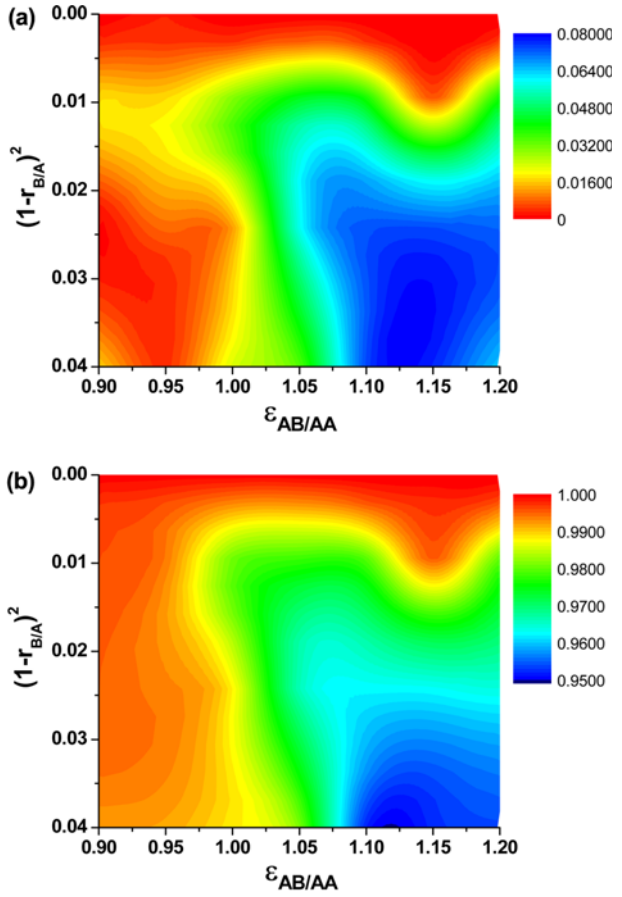

Fig. 5. (a) Fraction of the icosahedron-centered atom (F_{ico}) after the quenching process. (b) Ratio of the atomic distance between a smaller atom and neighboring atoms after the quenching process:

$$\text{Ratio} = \frac{\left(1-\frac{C_{AB}}{C}\right)r_{B-B}+\frac{C_{AB}}{C}r_{B-A}}{\left(1-\frac{C_{AB}}{C}\right)^2 r_{B-B}+\frac{C_{AB}}{C}\left(1-\frac{C_{AB}}{C}\right)r_{B-A}+\left(1-\frac{C_{AB}}{C}\right)\frac{C_{AB}}{C}r_{A-A}+\left(1-\frac{C_{AB}}{C}\right)^2 r_{A-B}}$$

Here C is the coordination number, C_{AB} is the partial coordination number of element B around element A and r_{i-j} is the interatomic distance from the i atom to the j atom.

5. CONCLUSIONS

As far as we know, this study is the first to determine the general behavior of metallic glasses as a function of adjustable potential parameters of the atomic size and potential well-depth base on LJ-EAM models. The conclusions are given below.

(1) An effective heat of mixing makes the following two contributions: the chemical contribution related to the bond energy difference and the misfit strain energy contribution related to the atomic size difference.

(2) A positive heat of mixing causes liquid phase separation, thus reducing the GFA by removing the effect of the atomic size difference, while a negative heat of mixing contributes to the preferred formation of a chemical bond between unlike atoms.

(3) A large atomic size difference contributes to an increase in the energy of the crystalline phase, resulting in the destabilization of the crystalline phase and the formation of an icosahedral local structure.

(4) A larger atomic size difference and the accompanying negative heat of mixing sufficient to prevent phase separation are necessary to enhance the GFA.

ACKNOWLEDGEMENTS

This study was supported by the Global Research Laboratory Program of the Korea Ministry of Education, Science and Technology. Y. S. Yun is grateful for the support from the Third Stage of Brain Korea 21 Project in 2012. H.-S. Nam and P.-R. Cha acknowledge support from the Priority Research Centers Program through the National Research Foundation (NRF) (2009-0093814).

REFERENCES

1. A. Inoue, *Mater. Trans. JIM*. **36**, 866 (1995).
2. J. H. Li, Y. Dai, Y. Y. Cui, and B. X. Liu, *Mater. Sci. Eng. R: Rep.* **72**, 1 (2011).
3. O. N. Senkov and D. B. Miracle, *Mater. Res. Bull.* **36**, 2183

(2001).
4. Z. P. Lu, C. T. Liu, and Y. D. Dong, *J. Non-Cryst. Solids*. **341**, 93 (2004).
5. J. Saida, M. Matsushita, and A. Inoue, *Mater. Trans.* **43**, 1937 (2002).
6. M. Shimono and H. Onodera, *Mater. Trans.* **46**, 2830 (2005).
7. J. J. Lee, K. W. Park, D. H. Kim, and E. Fleury, *Korean J. Met. Mater.* **49**, 930 (2011).
8. H.-S. Kim, K.-S. Yoon, and J.-C. Lee, *Korean J. Met. Mater.* **49**, 823 (2011).
9. V. V. Hoang, *Physica B: Condensed Matter* **406**, 3653 (2011).
10. M. Shimono and H. Onodera, *Mater. Trans.* **45**, 1163 (2004).
11. M. Shimono and H. Onodera, *Scripta Mater.* **44**, 1595 (2001).
12. J. M. Delaye and Y. Limoge, *J. Non-Cryst. Solids* **156-158**, 982 (1993).
13. P. M. Derlet, R. Maaß, and J. F. Löffler, *Eur. Phys. J. B* **85**, 148 (2012).
14. D. Wang, Y. Li, B. B. Sun, M. L. Sui, K. Lu, and E. Ma, *Appl. Phys. Lett.* **84**, 4029 (2004).
15. D. Xu, B. Lohwongwatana, G. Duan, W. L. Johnson, and C. Garland, *Acta Mater.* **52**, 2621 (2004).
16. M. B. Tang, D.-Q. Zhao, M.-X. Pan, and W.-H. Wang, *Chinese Phys. Lett.* **21**, 901 (2004).
17. N. Mattern, P. Jóvári, I. Kaban, S. Gruner, A. Elsner, V. Kokotin, H. Franz, B. Beuneu, and J. Eckert, *J. Alloys Comp.* **485**, 163 (2009).
18. A. E. Lagogianni, G. Almyras, Ch. E. Lekka, D. G. Papageorgiou, and G. A. Evangelakis, *J. Alloys Comp.* **483**, 658 (2009).
19. G. A. Almyras, Ch. E. Lekka, N. Mattern, and G. A. Evangelakis, *Scripta Mater.* **62**, 33 (2010).
20. L. Yang, S. Yin, X. D. Wang, Q. P. Cao, J. Z. Jiang, K. Saksl, and H. Franz, *J. Appl. Phys.* **102**, 083512 (2007).
21. D. Holland-Moritz, S. Stüber, H. Hartmann, T. Unruh, T. Hansen, and A. Meyer, *Phys. Rev. B* **79**, 064204 (2009).
22. E. W. Iparraguirre, J. Sietsma, and B. J. Thijsse, *J. Non-Cryst. Solids* **156**, 969 (1993).
23. H. Ruppersberg, D. Lee, and C. N. J. Wagner, *J. Phys. F-Met. Phys.* **10**, 1645 (1980).
24. L. Pusztai and E. Svab, *J. Non-Cryst. Solids* **156**, 973 (1993).
25. E. Svab, F. Forgács, F. Hajdu, N. Kroó, and J. Takács, *J. Non-Cryst. Solids* **46**, 125(1981).
26. M. Sakata, N. Cowlam, and H. A. Davies, *J. Phys. F-Met. Phys.* **11**, L157 (1981).
27. L. Zhang, Y.-Q. Cheng, A.-J. Cao, J. Xu, and E. Ma, *Acta Mater.* **57**, 1154 (2009).
28. T. Takagi, T. Ohkubo, Y. Hirotsu, B. S. Murty, K. Hono, and D. Shindo, *Appl. Phys. Lett.* **79**, 485 (2001).
29. D. J. Sordelet, R. T. Ott, M. Z. Li, S. Y. Wang, C. Z. Wang, M. F. Besser, A. C. Y. Liu, and M. J. Kramer, *Metall. Mater. Trans. A-Phys. Metall. Mater. Sci.* **39A**, 1908 (2008).
30. Y. Q. Cheng and E. Ma, *Prog. Mater. Sci.* **56**, 379 (2011).
31. Y. Q. Cheng, E. Ma, and H. W. Sheng, *PRL* **102**, 245501 (2009).
32. Y. Q. Cheng, E. Ma, and H. W. Sheng, *Appl. Phys. Lett.* **93**, 111913 (2008).
33. S. G. Srinivasan and M. I. Baskes, *Proc. R. Soc., Lond., Ser. A* **460**, 1649 (2004).
34. A. Oluwajobi and X. Chen, *Key Eng. Mater.* **535-536**, 330 (2013).
35. R. K. Rajgarhia, D. E. Spearot, and A. Saxena, *Comp. Mater. Sci.* **44**, 1258 (2009).
36. R. B. Godiksen, Z. T. Traut, M. Upmanyu, S. Schmidt, and D. J. Jensen, *Mater. Sci. Forum* **558-559**, 1081 (2007).
37. X.-L. Ma and W. Yang, *Nanotechnology* **15**, 449 (2004).
38. Z. Guo and W. Yang, *Int. J. Mech. Sci.* **48**, 145 (2006).
39. B. Ao, X. Wang, W. Hu, and J. Yang, *Phys. Status Solidi B* **245**, 1493 (2008).
40. B. Ao, X. Wang, W. Hu, and J. Yang, *J. Nucl. Mater.* **385**, 75 (2009).
41. Y. Yonekawa and K.-I. Saitoh, *Zairyo/Journal of the Society of Materials Science*, **59**, 624 (2010).
42. S. Davis, C. Loyola, F. González, and J. Peralta, *Comput. Phys. Commun.* **181**, 2126 (2010).
43. H. Kang Y. Zhang, and M. Yang, *Appl. Phys. A* **103**, 1001 (2011).
44. H. Tsuzuki, P. S. Branicio, and J. P. Rino, *Comput. Phys. Commun.* **177**, 518 (2007).
45. A. Takeuchi and A. Inoue, *Mater. Trans.* **46**, 2817 (2005).